Electronic Supplementary Material (ESI) for Sustainable Energy & Fuels.

Supporting Information

Directly Fabricated Phosphorus-Doped Nickel Sulfide and Eco-Friendly Biomass-Derived Humic Acid as Efficient Electrodes for Energy Storage Application

Farzaneh Hekmat[a], Mahdiyeh Shahi[a], Saeed Shahrokhian[a,b]

[a] *Department of Chemistry, Sharif University of Technology, Azadi Avenue, Tehran 11155-9516, Iran*

[b] *Institute for Nanoscience and Nanotechnology (INST), Sharif University of Technology, Azadi*

EDS Spectrums of the Positive Electrodes

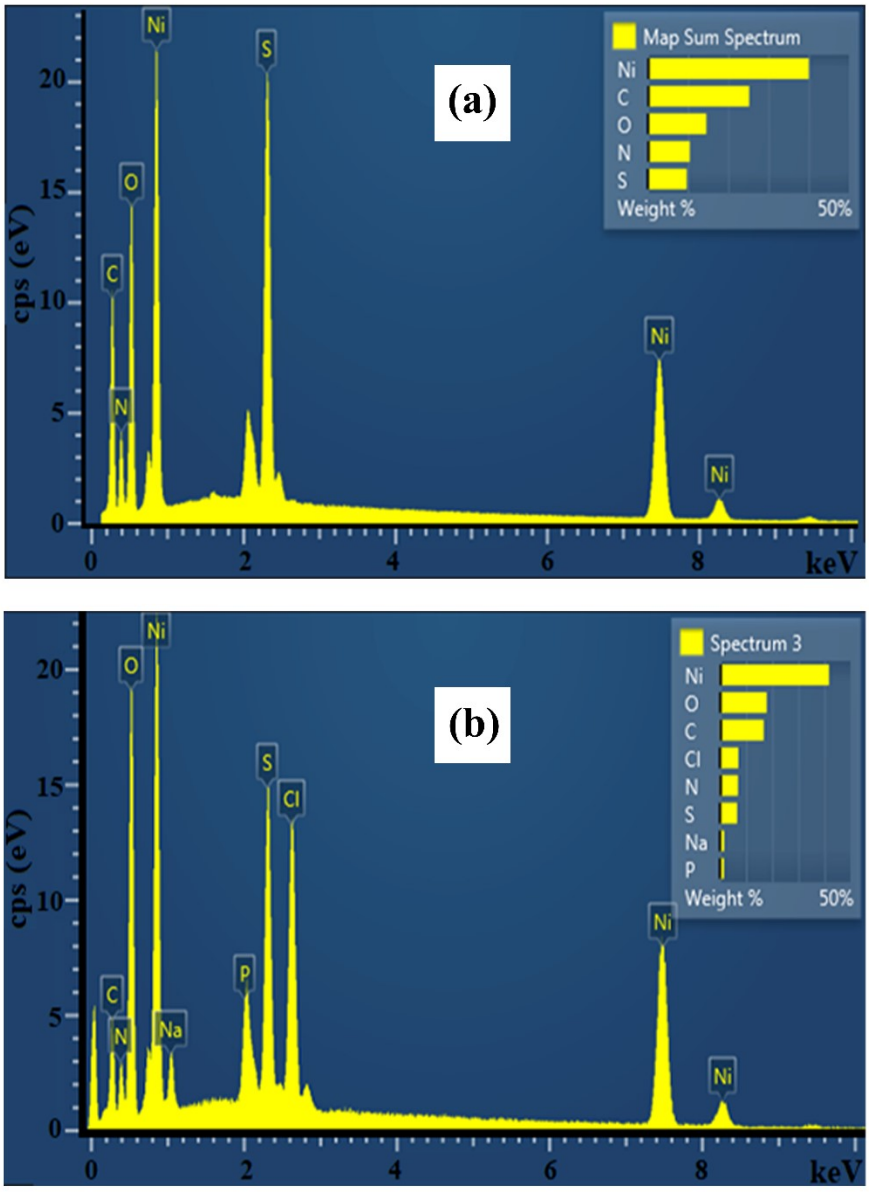

Fig. S1. (a) EDS results of the NiS-NF, and (b) P-doped NiS-NF

XPS Measurements of P-doped NiS-NFs

The surface chemical composition and valence states of the P-doped NiS-NFs were further evaluated using XPS measurements. The XPS survey spectrum, as well as the corresponding high-resolution de-convoluted spectra of the Ni, O, P, and S are shown in Fig. S2. The

characteristic peaks of Ni, P, and S were observed in the wide survey spectrum (Fig. S2 (a)). As seen in Fig. S2 (b) the high-resolution XPS spectrum of Ni 2p was best fitted with two spin-orbit doublets and two satellite peaks, which were observed at 874.3, 856.0, 880.4, and 862.3 eV, respectively [1]. The observation of these pairs of the satellite peaks together with the spin-orbits provide evidence on the coexistence of both Ni^{+2} and Ni^{+3} in the prepared P-doped NiS nanostructures [1]. As a direct consequence of P-doping, electron density around Ni cations was decreased. A slight shift of the Ni 2p characteristic peaks into the higher binding energies, in turn, is observed in Fig. S2(b) [2]. The S 2p spectrum can be also fitted into two peaks at 164.8 and 162.5, which can be assigned to S $2p_{1/2}$ and S $2p_{3/2}$, respectively (Fig. S2 (c)) [1]. Two weak peaks centered at 168.3 and 160 eV can be attributed to the sulfide species possibly generated by the oxidation of sulfides in air and metal-S bonds, respectively [2]. In good agreement with the Ni 2p de-convoluted spectrum, a slight shift has also come into view in the de-convoluted spectrum of S 2p. As seen in Fig. S2(d), two sharp peaks at binding energies of 124.0 and 128.8 eV are observed in the de-convoluted XPS spectrum of P 2p. These two peaks can be assigned to P $2p_{3/2}$ and $2p_{1/2}$, which are assigned to the successful formation of metal-phosphide bonds [2]. Besides, when exposed to air, the surface oxidation of metal phosphides resulted in the observation of a relatively strong peak at 133.3 eV. In good agreement with the XRD and FT-IR results, the successful incorporation of phosphides into the nickel sulfide nanostructures is evidenced by XPS outputs.

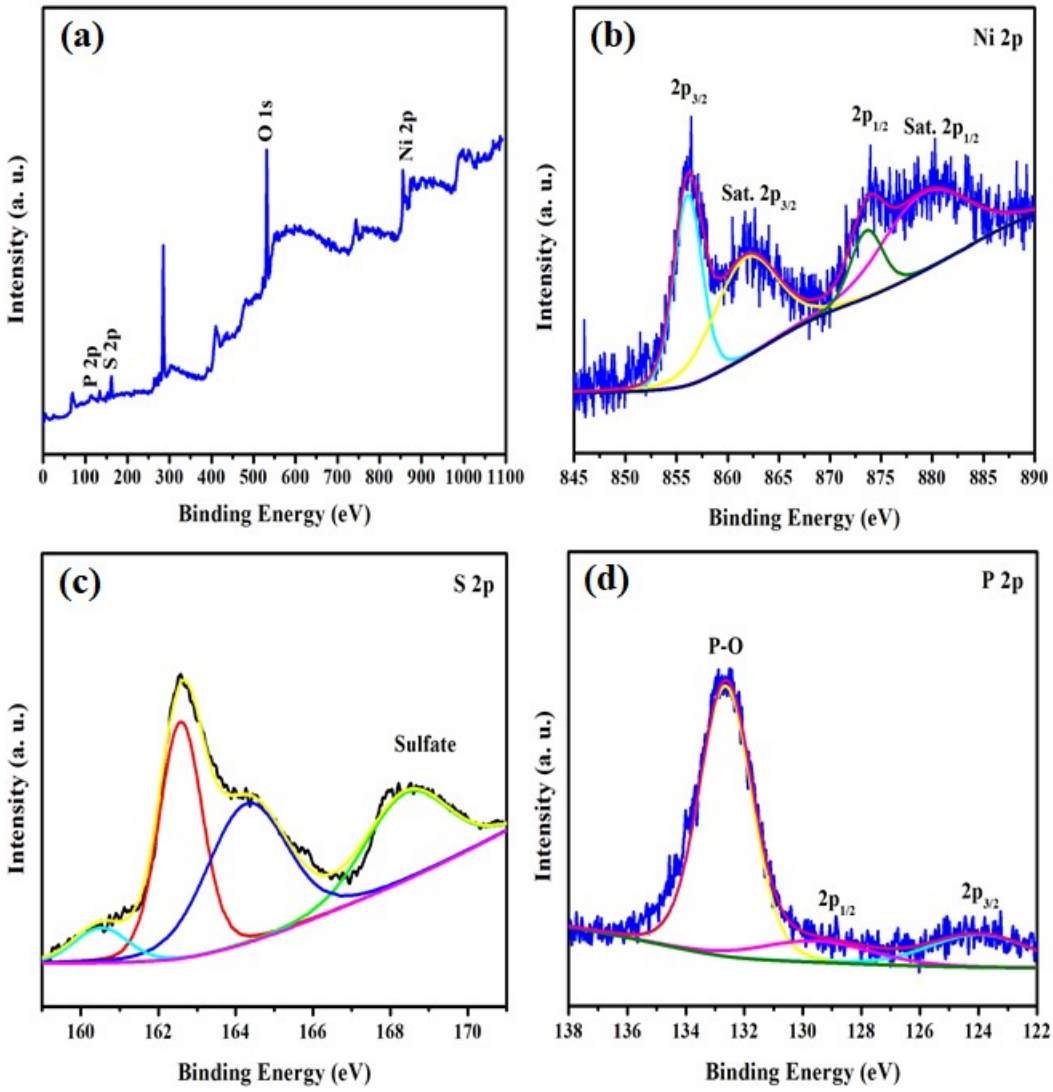

Fig. S2. (a) The XPS survey scan and XPS de-convoluted spectra of (b) Ni 2p, (c) S 2p, and (d) P 2p.

XRD Characterization of the Positive Electrodes after Cycle Stability Estimation

To find more information about the mechanism of the activation process in the alkaline media (3M KOH), the microstructure and composition of the positive electrodes were further characterized using XRD analysis. Accordingly, the electrode active materials were collected after 10000 continuous charge-discharge cycles. As seen in Fig. S3, P-doped Nickel sulfides were mostly converted into NiO nanostructures via an in-situ process.

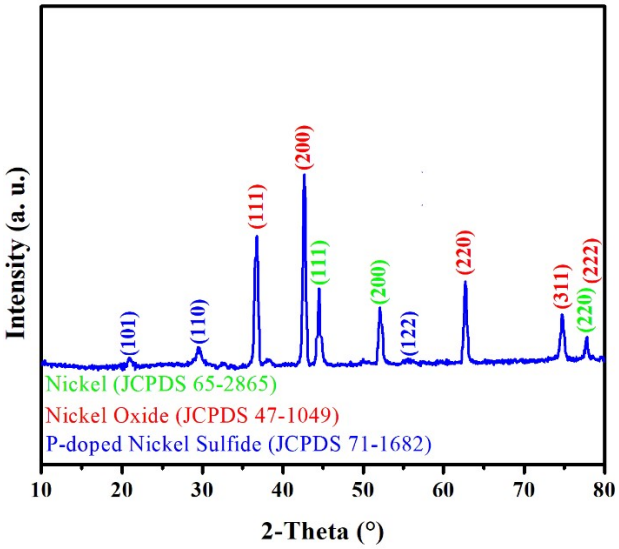

Fig. S3. XRD pattern of the P-doped NiS-NFs after 10000 continuous charge-discharge cycles.

The Nyquist plot of the Positive Electrodes after Cycle Stability Estimation and Bode Plot of the Positive Electrode Before and After Cycle Stability Estimation

The charge transfer process at the electrode/electrolyte interface of the positive electrodes was further investigated after 10000 charge-discharge cycles. The Nyquist plots of the positive electrodes and their corresponding enlargements of the high-frequency region alongside the corresponding equivalent circuit model, derived from EIS analysis, are provided in Fig. S4(a). As seen in the figure, the semicircles at high frequencies are followed by a quasi-vertical line at low frequencies. Due attention to the first real axis intercept of the Nyquist plot, the internal resistance of the electrodes can be estimated about 1.83 Ω. Besides, as a direct consequence of the fast charge transport rate (R_{ct} = 0.75 Ω), a narrow semicircle was observed in the high-frequency region. Additionally, the Bode phase diagrams of the positive electrode (before and after cycle stability estimation) are provided in Fig. S4(b). As seen in the figure, after 10000 charge-discharge GCD cycles, the phase angle of the positive electrodes is reduced from 75 to 60°. As it is known, the closer the phase angle approaches 90° provides evidence that the

electrode has the merit of the better capacitive performance. Accordingly, the electrochemical performance of the prepared electrodes was slightly declined under continuous charge-discharge cycles. Besides, the relaxation time constant ($\tau_0 = 1/f_0$), which is the minimum time required to discharge all the energy from the device with an efficiency greater than 50%, provides evidence on the remarkable ion diffusion, rate capability, and power density of the P-doped NiS-NFs.

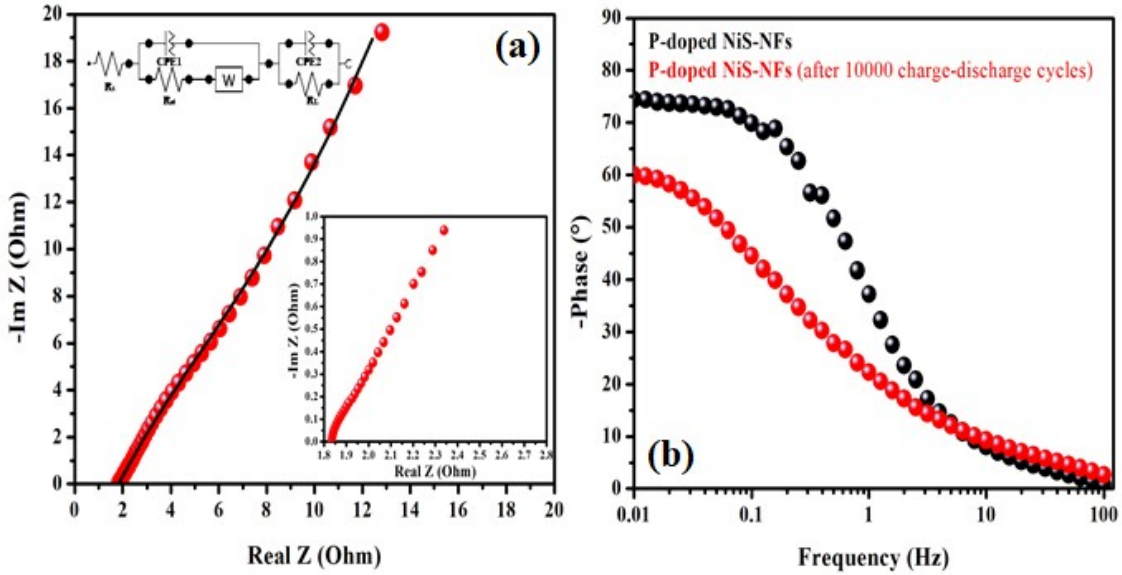

Fig. S4. (a) The Nyquist plot, inset: the magnified high-frequency region and the equivalent circuit of the P-doped NiS-NFs after 10000 continuous charge-discharge cycles and (b) the Bode plots of the positive electrodes obtained before and after 10000 charge-discharge cycles.

EDS Spectrums of the Negative Electrodes

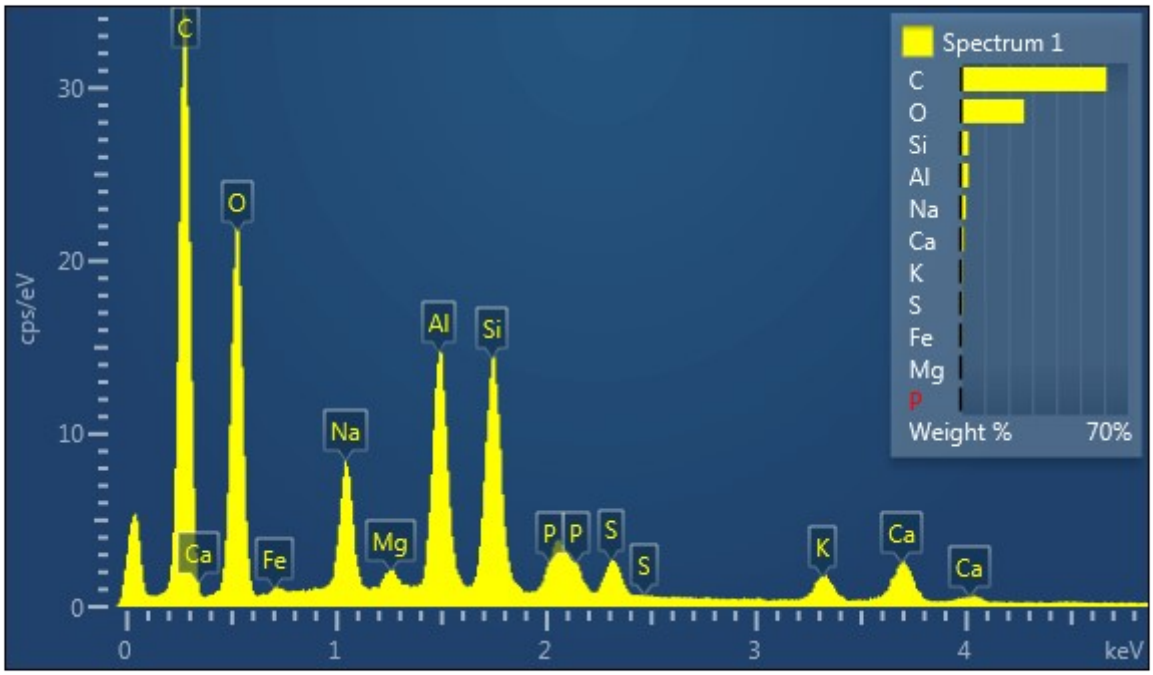

Fig. S5. EDS results of the A-HA

XRD Characterization of the Negative Electrodes after Cycle Stability Estimation

The microstructure and composition of the negative electrodes were also investigated after electrochemical activation under an alkaline condition (Fig. S6). In comparison to the A-HAs, the XRD pattern of the electrode active materials, obtained after activation in 3M KOH, provides evidence that the SiO_2 was partially converted into the K_2SiO_3, which is soluble in the water.

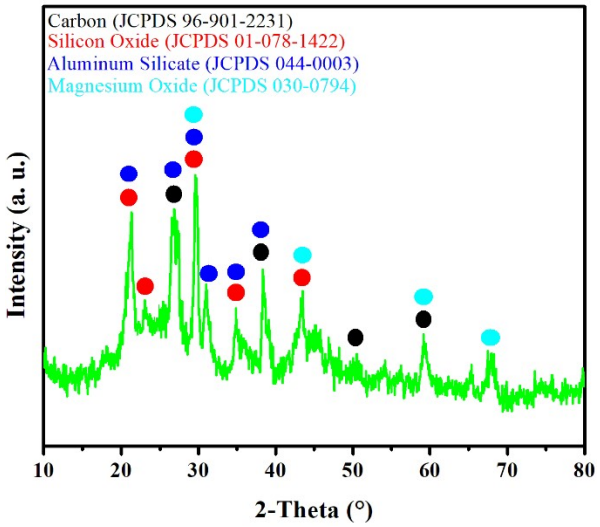

Fig. S6. XRD pattern of the A-HA-NFs after 10000 continuous charge-discharge cycles

The Nyquist plot of the Negative Electrodes after Cycle Stability Estimation and Bode Plot of the Negative Electrode Before and After Cycle Stability Estimation

The charge transfer mechanism was also evaluated by measuring the frequency response of the A-HA-NFs after 10000 continuous charge-discharge cycles and the results were provided in Fig. S7. As seen in the Nyquist plot, which is provided in Fig. S7(a), the activated electrodes receive benefits from a negligible ESR (~1.04 Ω) and a fast charge transfer rate (R_{ct} = 1.12 Ω). The Nyquist plot was found to be in good agreement with the results derived from XRD structural measurements conducted after 10000 charge-discharge cycles. This indicates that the partially dissolving of the SiO_2 nanostructures, preventing carbon nanosheets from sticking, resulted in less accessible channels for the electrolyte ion diffusion. Compared to the A-HA-NFs (Fig. 9(b)), the higher ESR and R_{ct}, in turn, were observed for the activated negative electrodes after 10000 charge-discharge cycles.

Besides, the Bode phase diagrams of the A-HA-NFs (before and after cycle stability estimation) are provided in Fig. S7(b). As seen in the figure, after 10000 charge-discharge GCD cycles, the phase angle of the negative electrodes is reduced from 81 to 67. The electrochemical performance of the prepared electrodes, in this regard, was slightly deviated from ideal capacitors under continuous charge-discharge cycles in an alkaline condition. In addition, the relaxation time constant of the negative electrodes indicates that the fabricated negative electrodes receive benefits from considerable ion diffusion, rate capability, and power density.

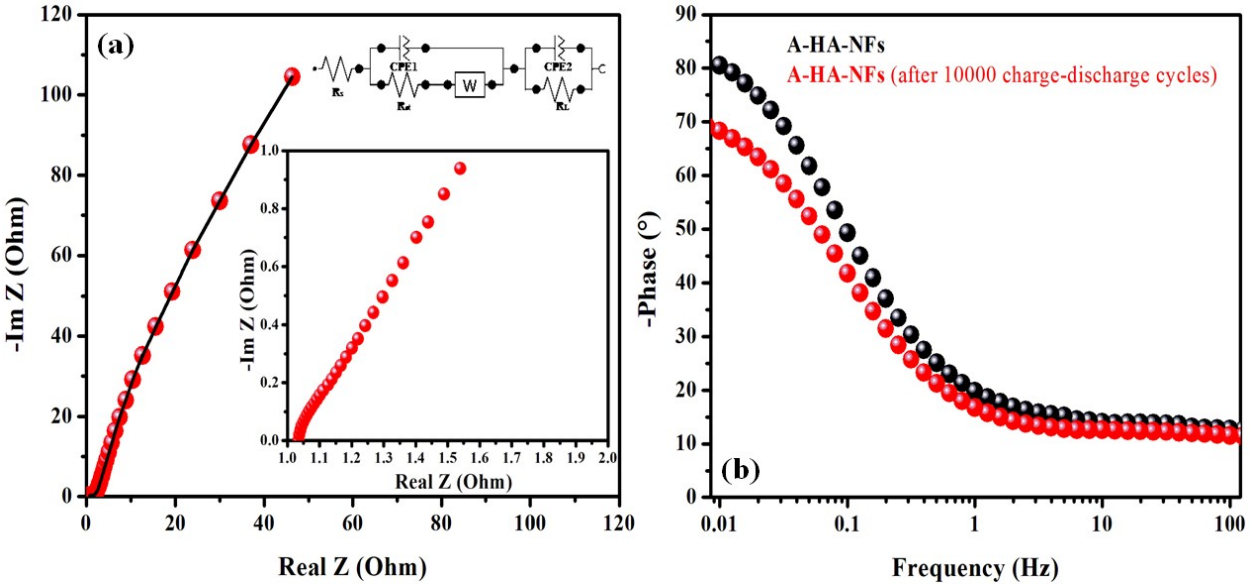

Fig. S7. (a) The Nyquist plot, inset: the magnified high-frequency region and the equivalent circuit of the A-HA-NFs after 10000 continuous charge-discharge cycles and (b) the Bode plots of the positive electrodes obtained before and after 10000 charge-discharge cycles.

Electrode and ASCs Device Properties Comparison with Reported Literature

Table S1. Electrode properties comparison with the reported literature.

Electrode Materials	Electrolyte	C_{sp} or Q (F/g)	Current Load (A/g)	Cycle Stability	Ref. No
NiS/NF	KOH (2M)	2.64 F/cm^2 (at 2.5 mA/cm^2)	2.5-100 (mA/cm^2)	90% (after 2000 cycles)	3
Ni_2P/NiS_2	KOH (2M)	212.7* (at 2 A/g)	2-20	83.6% (after 5000 cycles)	4
Ni_3S_2@C/rGO	KOH (2M)	1023.44 (at 5 A/g)	5-20	70.1% (after 5000 cycles)	5
Ni_3S_4 3D frames	KOH (3M)	1213 (at 2 A/g)	2-12	60% (after 2000 cycles)	6
NiS_2/pCMT	$LiPF_6$ (1M) in (EC/DMC/DEC)	1086* (at 0.1 A/g)	0.1-8	88% (after 5000 cycles)	7
NiP	KOH (2M)	136.22* (at 0.5 A/g)	0.5-10	81% (after 3000 cycles)	8
NiCoP@NiCoP-CC	KOH (3M)	312 (at 1 A/g)	1-10	71.8% (after 2000 cycles)	9
TWPC	KOH (6M)	332 (at 1 A/g)	1-100	97.8% (after 100000 cycles)	10
SPC	H_2SO_4 (1M)	398 (at 0.4 A/g)	0.4-6	-	11
P-doped NiS-NF	KOH (3M)	486.7* (at 6 A/g)	6-50	82.9% (after 10000 cycles)	This work
A-HA-NF	KOH (3M)	164.2 (at 0.1 A/g)	0.1-5	88.7% (after 10000 cycles)	This work

*Due to the battery-type behavior of the electrodes, the concept of capacity ($mAh.g^{-1}$) was used instead of capacitance (Fg^{-1}) as an appropriate metric for the battery-like electrodes.

pCMTs=porous carbon microtubes, EC/DMC/DEC=ethylene carbonate/dimethyl carbonate/diethyl carbonate, SPC=sulfonated porous carbon nanosheets, TWPC=tea waste porous carbon,CC=carbon cloth.

Table S2. Comparative table of electrochemical properties of the fabricated ASC devices with the literature.

Electrode		**Electrolyte**	**C_{sp} or Q (F/g)**	**E_{max} (Wh/kg)**	**P_{max} (kW/kg)**	**Cycle Stability**	**Ref. No**
Positive	**Negative**						
NiS/NF	AC	KOH (2M)	107.9 (at 2.5 mA/cm^2)	38.4	0.167	90.6% (after 1000 cycles)	3
Ni_3S_2@C/rGO	AC	KOH (2M)	168 (at 1 A/g)	52.5	7.5	99.28% (after 1000 cycles)	5
NiS_2/pCMT	AC	$LiPF_6$ (1M) in (EC/DMC/DEC)	450 (at 1 A/g)	136	-	83% (after 5000 cycles)	7
NiCoP@NiCoP-CC	AC	KOH (3M)	167* (at 1 A/g)	34.8	7.5	81.2% (after 10000 cycles)	9
SPC	SPC	Na_2SO_4 (1M)	124 (at 0.1 A/g)	17	3.333	97% (after 10000 cycles)	11
P-doped NiS-NF	A-HA-NF	KOH (3M)	103.8* (at 0.18 A/g)	36.32	6.921	78.4% (after 10000 cycles)	This work

*Due to the battery-type behavior of the fabricated devices, the concept of capacity ($C.g^{-1}$) was used instead of capacitance (Fg^{-1}) as an appropriate metric for the battery-like devices, SPC=sulfonated porous carbon nanosheets.

C_{sp}=Specific Capacitance, Q=Specific Capacity, E_{max}= Max Energy Density, P_{max}= Max Power Density, MSs= microspheres, AC=Activated Carbons, NPs=Nanoparticles, NGN=Nitrogen-doped Graphene, CNTs=Carbon Nanotubes, NW=Nanowires, rGO=Reduced Graphene Oxide, HTCSs=Hydrothermal Carbon Spheres, PPNT=Pyrolyzed Polyaniline Nanotubes, PANI=Poly aniline, HPCT=Hierarchical porous and N-doped carbon nanotubes derived from polyaniline, CS=Carbon Sphere, VO=Vanadium Oxide.

References

[1] F. Hekmat, M. Ezzati, S. Shahrokhian, H.E. Unalan, J. Electroanal. Chem. 890 (2021) 115244.

[2] W. He, D. Jia, J. Cheng, F. Wang, L. Zhang, Y. Li, C. Liu, Q. Hao, J. Zhao, Catal. Sci. Technol. 10 (2020) 7581–7590.

[3] L. Yu, B. Yang, Q. Liu, J. Liu, X. Wang, D. Song, J. Wang, X. Jing, J. Electroanal. Chem. 739 (2015) 156–163.

[4] J. Gou, J. Electrochem. Soc. 164 (2017) A2956–A2961.

[5] J. He, C. Guo, S. Zhou, Y. Zhao, Q. Wang, S. Yang, J. Yang, Q. Wang, Inorg. Chem. Front. 6 (2019) 226–232.

[6] L. Wang, J. Liu, L.L. Zhang, B. Dai, M. Xu, M. Ji, X.S. Zhao, C. Cao, J. Zhang, H. Zhu, RSC Adv. 5 (2015) 8422–8426.

[7] J. Zhao, G. Wang, K. Cheng, K. Ye, K. Zhu, J. Yan, D. Cao, H.-E. Wang, J. Power Sources 451 (2020) 227737.

[8] V.T. Chebrolu, B. Balakrishnan, S. Aravindha Raja, I. Cho, J.-S. Bak, H.-J. Kim, New J. Chem. 44 (2020) 7690–7697.

[9] Y. Zhu, Q. Zong, Q. Zhang, H. Yang, Q. Wang, H. Wang, Electrochim. Acta 299 (2019) 441–450.

[10] A. Khan, R.A. Senthil, J. Pan, S. Osman, Y. Sun, X. Shu, Electrochim. Acta 335 (2020) 135588.

[11] A. Gopalakrishnan, S. Badhulika, Renew. Energy 161 (2020) 173–183.